CrystEngComm

PAPER

View Article Online
View Journal | View Issue

Cite this: *CrystEngComm*, 2024, **26**, 2526

Structural diversity and tetrel bonding significance in lead(II) complexes with pyrazoylisonicotinoylhydrazone and varied anionic co-ligands†

Ghodrat Mahmoudi, [ab] Isabel García-Santos, *[c] Roi Fernández-Vázquez,[c] Rosa M. Gomila, [d] Alfonso Castiñeiras, [c] Esmail Doustkhah, [b] Ennio Zangrando [e] and Antonio Frontera *[d]

Four lead(II) complexes featuring pyrazoylisonicotinoylhydrazone ligand paired with various anionic co-ligands (azido, thiocyanato, nitrito, and nitrato) were synthesized and thoroughly examined using structural, analytical, and spectroscopic techniques. These ligands, in their mono-deprotonated state, bind to the lead(II) ion in a tridentate manner through two nitrogen atoms and one oxygen atom. Single-crystal X-ray crystallography revealed the capacity of these molecular complexes to form larger aggregates influenced by the nature of the anion attached to the metal center. In every complex, the lead atom adopts a hemidirectional coordination environment, making it geometrically suited for tetrel bond formation. The crystal structures demonstrate that lead atoms engage in notably short interactions with nitrogen atoms, distances that are shorter than the sum of their van der Waals radii yet exceed the sum of their covalent radii. These tetrel bonds play a pivotal role in weaving the monomeric into self-assembled dimers or extended supramolecular 1D polymers. The formation and characteristics of these intriguing supramolecular structures observed in the solid state of each complex were further explored and validated through density functional theory (DFT) calculations and several computational tools like MEP, NCIPlot, QTAIM, and ELF methods.

Received 3rd April 2024,
Accepted 11th April 2024

DOI: 10.1039/d4ce00325j

rsc.li/crystengcomm

Introduction

Non-covalent interactions are fundamental to the architecture, functionalities, and behaviour of a wide array of materials, spanning from intricate biochemical systems to simple chemical compounds and cocrystals.[1,2] Among the most recognized non-covalent forces are hydrogen bonds, van der Waals' interactions, and π-stacking, which have long been acknowledged for their pivotal roles in molecular assembly and structural integrity.[3–8] In the realm of chemical science, halogen bonds have emerged as a subject of increasing interest and investigation in recent years.[9,10] Defined as the attractive force between an electrophilic halogen atom region in one molecular entity and a nucleophilic region in another or the same molecular entity, halogen bonding has broadened our understanding of molecular interactions.[11]

Expanding on this concept, Cavallo *et al.*[12] have introduced a framework for categorizing interactions based on the nature of the electrophilic site involved.[13] This includes pnictogen bonds,[14] chalcogen bonds,[15] tetrel bonds,[16] and aerogen bonds,[17] among others, thus enriching the vocabulary of non-covalent bonding in chemistry. Each of these interactions offers unique perspectives on how molecules associate and assemble, influencing their structural, electronic, and dynamic properties.

The evolution of these concepts requires rigorous scholarly examination. The precise characterizations and

[a] *Department of Chemistry, Faculty of Science, University of Maragheh, P.O. Box 55136-83111, Maragheh, Iran*
[b] *Chemistry Department, Faculty of Engineering and Natural Sciences, Istinye University, Sariyer, Istanbul 34396, Turkey*
[c] *Departamento de Química Inorgánica, Facultad de Farmacia, Universidad de Santiago de Compostela, E-15782 Santiago de Compostela, Spain. E-mail: isabel.garcia@usc.es*
[d] *Department of Chemistry, Universitat de les Illes Balears, Crta de Valldemossa km 7.5, 07122 Palma de Mallorca, Baleares, Spain*
[e] *Department of Chemical and Pharmaceutical Sciences, University of Trieste, Via L. Giorgieri 1, 34127 Trieste, Italy*

† Electronic supplementary information (ESI) available: Tables S1 to S3. CCDC 2339688–2339691. For ESI and crystallographic data in CIF or other electronic format see DOI: **https://doi.org/10.1039/d4ce00325j**

theoretical underpinnings of such non-covalent bonds are subjects of ongoing research. In this vein, a notable initiative by the International Union of Pure and Applied Chemistry (IUPAC) aims to categorize these interactions formally. The project, entitled "Categorizing Chalcogen, Pnictogen, and Tetrel Bonds, and Other Interactions Involving Groups 14–16 Elements",[18] seeks to establish clear definitions and criteria for these bonds. Through this endeavour, IUPAC aims to standardize the terminology and understanding of these crucial interactions, reflecting the growing recognition of their significance in chemistry and material science. This effort underscores the dynamic nature of the field, where new discoveries and insights continuously reshape our comprehension of this topic.

Electron-deficient areas, known as σ-holes, are notably found on the covalently bonded heavier atoms of groups 14 to 18, extending directly from the covalent bonds.[19] The characteristics of these σ-holes, specifically their size and degree of electron deficiency, are influenced by the electron-withdrawing capacity of the attached group and the polarizability of the atom hosting the σ-hole.[20–22] While σ-hole interactions have been extensively explored for groups 17–15, those involving group 14 (tetrel bonding interactions) have been less frequently reported.[23] Nonetheless, studies have demonstrated their considerable strength, especially involving tin and lead, the metal constituents of group IV.[24] Our research team and others have previously contributed to this field by designing and synthesizing lead(II) metal–organic frameworks (MOFs) that utilize both covalent and noncovalent tetrel bonding mechanisms.[25,26] In these structures, noncovalent Pb···S and Pb···N tetrel bonds play a crucial role in linking the covalently bonded components into larger supramolecular assemblies. Further investigation has underscored the significant and predictable presence of tetrel bonds in lead's solid-state chemistry, particularly when lead is hemidirectionally coordinated.[27–33] It has also been demonstrated that solid-state ^{207}Pb NMR spectroscopy is a valuable tool in studying compounds featuring lead tetrel bonds.[34]

In this manuscript we report the synthesis and spectroscopic characterization of four lead(II) complexes with tridentate pyrazoylisonicotinoylhydrazone ligand and different anionic co-ligands (azido, thiocyanato, nitrito, and nitrato). Single-crystal X-ray crystallography showed that these complexes can aggregate into larger structures, depending on the coordinated anion. The lead atom's hemidirectional coordination is conducive to tetrel bond formation, evident in short Pb···N,O,S interactions within the structures. These tetrel bonds are crucial for forming dimers and 1D supramolecular polymers, as confirmed by density functional theory (DFT) calculations and other computational analyses, including MEP, NCIPlot, QTAIM, and ELF methods. This manuscript highlights the multifaceted roles of tetrel bonding in defining molecular structures.

Experimental

Materials and physical measurements

All reagents used in these studies were obtained from commercial sources and used as received. **HL**s were prepared as reported.[33] The FTIR spectra in the KBr pellets were obtained with an F_T 801 spectrometer. Microanalyses were performed using a LECO-elemental analyzer.

Synthesis and characterization of 1–4

[Pb(L)(N_3)]. A suspension of $Pb(ClO_4)_2{\cdot}3H_2O$ (0.034 g, 0.084 mmol) and NaN_3 (0.011 g, 0.169 mmol) in water (2 mL) was added to a solution of **HL** (0.020 g, 0.084 mmol) in MeOH/CH_3CN (30 mL, 1 : 1). The resulting mixture was stirred for 0.5 h followed by filtration. After several days, single crystals were formed. Anal. calc. for $C_{11}H_9N_9PbO$ (490.46): C 26.94, H 1.85 and N 25.70%; found: C 26.85, H 1.84 and N 25.54%.

[Pb(L)(SCN)]. A suspension of $Pb(SCN)_2$ (0.027 g, 0.084 mmol) in water (2 mL) was added to a solution of **HL** (0.020 g, 0.083 mmol) in MeOH (30 mL). The resulting mixture was stirred for 0.5 h, followed by filtration. After several days, single crystals were formed. Anal. calc. for $C_{12}H_9N_7OPbS$ (506.51): C 25.98, H 1.78 and N 22.04%; found: C 25.90, H 1.72 and N 22.09%.

[Pb(L)(NO_2)]. A suspension of $Pb(NO_3)_2$ (0.029 g, 0.083 mmol) and $NaNO_2$ (0.012 g, 0.174 mmol) in water (2 mL) was added to a solution of **HL** (0.021 g, 0.083 mmol) in MeOH (30 mL). The resulting mixture was stirred for 0.5 h, followed by filtration. After several days, single crystals were formed. Anal. calc. for $C_{11}H_9N_7O_3Pb$ (494.44): C 26.72, H 1.83 and N 19.83%; found: C 26.81, H 1.85 and N 19.73%.

[Pb(L)(NO_3)]. A suspension of $Pb(NO_3)_2$ (0.028 g, 0.083 mmol) in water (2 mL) was added to a solution of **HL** (0.020 g, 0.083 mmol) in MeOH (30 mL). The resulting mixture was stirred for 0.5 h under reflux, followed by filtration. After several days, single crystals were formed. Anal. calc. for $C_{11}H_9N_7O_4Pb$ (506.51): C 25.88, H 1.78 and N 19.21%; found: C 25.80, H 1.82 and N 21.09%.

X-ray details

Single crystals of compounds **1–4** were mounted on a glass fiber, and diffraction data were collected at 250(2) K (complexes **1**, **4**) and 100(2) K (**2**, **3**) on a Bruker D8 Venture Photon III-14 diffractometer using graphite monochromated Mo-K_α radiation (λ = 0.71073 Å). Data reductions were performed with APEX3 software package,[35] and proper absorption corrections were applied to the data sets.[36] The structures were solved by direct methods with program SHELXS-2013 (ref. 37) and refined by full-matrix least-squares procedures using the SHELXTL program.[37] The hydrogen atoms were placed at calculated positions and constrained to ride to atoms to which they are attached, except those of amine groups of **2** that were located on the Fourier map and freely refined. Materials for publication were prepared using

Diamond 3.2k program[38] and WINGX package (Ver 2018.3).[39] Crystal data and details of refinements are reported in Table S1.† CCDC reference codes: 2339688–2339691.

Theoretical methods

The geometries of the complexes included in this study were computed at the PBE0-D3/def2-TZVP level of theory[40–42] using within the Gaussian-16 program.[43] The positions of the hydrogen atoms were optimized while the coordinates of the other atoms remained fixed. This level of theory includes dispersion correction, thus adequate for studying non-covalent interactions dominated by dispersion effects like π-stacking. The basis set superposition error for the calculation of interaction energies has been corrected using the counterpoise method.[44] The "atoms-in-molecules" (AIM)[45] analysis of the electron density has been performed at the same level of theory using the AIMAll program.[46] The 2D maps of Laplacian, reduced density gradient (RDG),[47] and ELF[48] were computed using Multiwfn program.[49]

Results and discussion

Structural description

Four novel pyrazoylisonicotinoylhydrazone (HL) Pb(II) complexes [Pb(L)X], where X = N3 (**1**), SCN (**2**), NO_2 (**3**), NO_3 (**4**), have been synthesized and structurally characterized by spectroscopic techniques and single crystal X-ray crystallography (see Scheme 1). In all cases, the ligand behaves as a tridentate species chelating the metal through the N/N/O donor set. The asymmetric unit of all the complexes comprises the Pb(II) atom chelated by the deprotonated tridentate ligand through the pyridine donor (N1), the aza nitrogen N2, and the carbonyl O1 atom, that form two five-membered rings, in addition to the coordinated anion—*i.e.*, azide, SCN, nitrite, and nitrate. Fig. 1 and 2 depict complexes **1**–**4** with an indication of long tetrel bonds of Pb(II) atom.

The Pb–O1, Pb–N1 and Pb–N2 bond lengths are close comparable in all structure falling in the ranges 2.338(5)–2.374(2), 2.7013(17)–2.780(6) and 2.375(3)–2.384(5) Å, respectively. The Pb–N (N_3), and Pb–NCS bond distance in complexes **1** and **2** are of 2.3862(19) and 2.374(3) Å, respectively. The azide and NCS anions are differently oriented with respect to the organic ligand with N–N–Pb and C–N–Pb bond angles of 120.36(15) and 138.1(3)°, respectively. On the other hand, in **3** and **4** the nitrite and nitrate anions

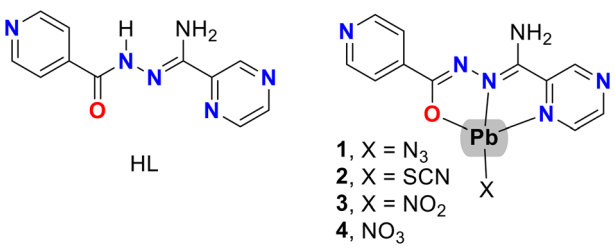

Scheme 1 Chemical drawings of the ligand (HL) and complexes **1**–**4**.

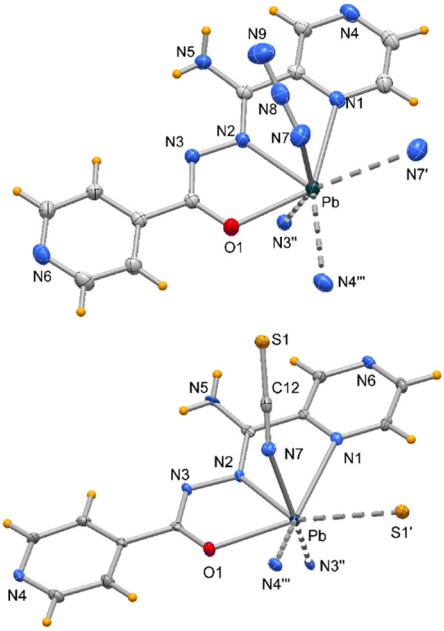

Fig. 1 Top: ORTEP drawing (ellipsoid probability at 50%) of complex **1**. Bottom: ORTEP drawing (ellipsoid probability at 50%) of complex **2**.

asymmetrically chelate the metal being Pb–O2 and Pb–O3 of 2.402 and 2.823 Å, respectively (mean values for the two complexes). The pyridine and pyrazine rings are almost coplanar, and the dihedral angle between them is larger (*ca.* 5.7(1)°) is observed in complex **1**, indicating an electron delocalization in all ligands. These geometrical parameters are in agreement with those measured in complexes with similar organic ligands.[50–53]

In each complex, the covalent bonds are concentrated on one side of the coordination sphere so as to leave a space on the Pb(II) ion, which enables a close approach with N, (O, or S) atoms of symmetry-related complexes (Fig. 1 and 2) as detailed reported in Table 1. These connections in complexes **1**, **2** and **4** comprise the pyrazine nitrogen N4 with Pb···N4 distances of 3.3724(19), 3.255(3) and 3.106(6) Å, respectively, while in complex **3** the pyrazine N4 is more distant at 3.781 Å. In addition, the metals in all species are separated from N3 of a complex related by an inversion center with Pb···N3 distances in a range of 3.064(6)–3.3662(17) Å.

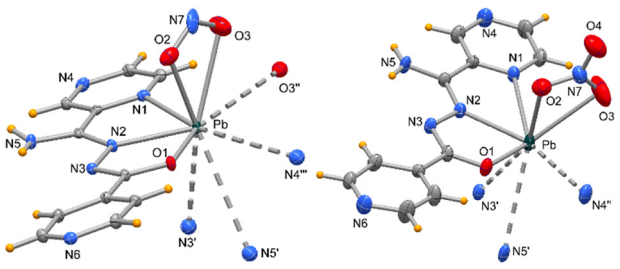

Fig. 2 Left: ORTEP drawing (ellipsoid probability at 50%) of complex **3**. Right: ORTEP drawing (ellipsoid probability at 40%) of complex **4**.

Table 1 Selected bond lengths and tetrel distances (Å) for complexes **1–4**

	1	2		3	4
Pb–O(1)	2.3600(14)	2.346(3)	Pb–O(1)	2.374(2)	2.338(5)
Pb–N(1)	2.7013(17)	2.717(3)	Pb–N(1)	2.720(3)	2.782(6)
Pb–N(2)	2.3765(16)	2.375(3)	Pb–N(2)	2.363(3)	2.384(6)
Pb–N(7)	2.3862(19)	2.374(3)	Pb–O(2)	2.411(3)	2.391(6)
Pb–N(7)$^{\#1}$	3.128(2)	—	Pb–O(3)	2.837(4)	2.808(9)
Pb–N(2)$^{\#2}$	3.7743(2)	3.452(3)	Pb–N(2)#1	3.437(3)	3.437(6)
Pb–N(3)$^{\#2}$	3.3662(17)	3.176(3)	Pb–N(3)#1	3.111(3)	3.064(6)
Pb–N(4)$^{\#3}$	3.3724(19)	3.255(3)	Pb–N(4)#2	3.781(3)	3.106(6)
Pb–S(1)$^{\#1}$	—	3.4175(11)	Pb–O(3)#2	3.557(3)	—

Symmetry codes: (**1**) #1 $-x+2, -y, -z+2$; #2 $-x+2, -y, -z+1$; #3 $x-1, y, z$; (**2**) #1 $-x, -y, -z+2$; #2 $-x, -y, -z+1$; #3 $x-1, y, z$; (**3**) #1 $-x+2, -y, -z+1$; #2 $-x+2, -y, -z+2$; (**4**) #1 $-x+2, -y, -z$; #2 $-x+2, y+1/2, -z+1/2$.

However, the presence of amino groups facilitates the formation of intermolecular H-bonds. In all cases the NH_2 interacts *via* hydrogen bond with the uncoordinated N6 of a symmetry related complex with comparable N5···N6 distances of 2.907(3), 2.919(5), 2.945(4) and 2.954(9) Å, in **1–4**, respectively. In complex **1** these N5–H···N6 interactions form a zig-zag 1D polymer in the crystallographic direction [201], while the second H is involved in an intramolecular interaction with N3, as displayed in Fig. 3. Each complex faces a counterpart correlated by an inversion center of adjacent polymers supporting π-stacking interactions between pyridine/pyrazine pairs (Fig. 3) as well as Pb···N3 tetrel bonds.

On the other hand, in **2–4**, the second hydrogen of the amino group interacts with atom S1 (in complex **2**) and with oxygen O2 in **3** and **4**. As result, the crystal packing of complex **2** shows the formation of undulated layers (Fig. 4) developed parallel to *ac* plane. More appealing are the crystal packings of complexes **3** and **4** realized by H-bond interactions that, as shown in Fig. 5 and 6, result in a double 2D polymeric layers of comparable topology with complexes centro-symmetrically paired that favor π-stacking interactions between pyridine and the pyrazine rings of symmetry-related complex. All the centroid-to-centroid distances between the heterocyclic rings fall in the range 3.545(1)–3.635(2) Å. Geometrical parameters of H-bonds and π···stacking interactions are reported in Tables S1 and S2,† respectively.

Theoretical study

Our theoretical investigation delved into the supramolecular assemblies observed in the solid states of complexes **1–4**, with a particular emphasis on the less conventional tetrel bonding and π-stacking interactions. For all complexes, we scrutinized the significant Pb···N,S,O interactions crucial for constructing self-assembled dimers and infinite 1D chains in their solid-state structures. Both interactions, in conjunction with H-bonds, are instrumental in driving the X-ray packing.

To further understand the donor–acceptor dynamics of the Pb(II) complexes, we calculated the molecular electrostatic potential (MEP) surfaces for compounds **1–4**, illustrated in Fig. 7 and 8. Intriguingly, for compounds **1** and **2**, the MEP surfaces revealed the most positive region at the NH_2 group (not shown in the perspective used in Fig. 7), while the most negative region was found on the pyridine's N atom rather than the expected pseudohalide ligand. This observation sheds light on the formation of the NH···N H-bonds. The MEP values are large and positive at the Pb-atom, showing three local MEP maxima approximately on the extension of three covalent Pb–O,N bonds.

Notably, the MEP surface analysis highlighted that MEP values over the center of pyridine and pyrimidine rings displayed contrasting signs, suggesting that the complexes will have a strong tendency to establish antiparallel π-stacking (electrostatically facilitated) between the coordinated pyrimidine and uncoordinated pyridine rings, as demonstrated in all

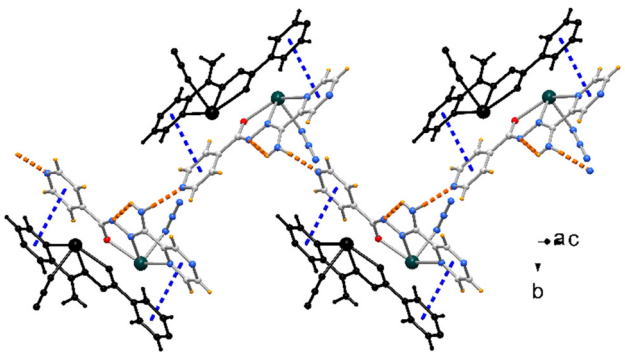

Fig. 3 1D polymeric chain formed by H-bond interactions in complex **1**.

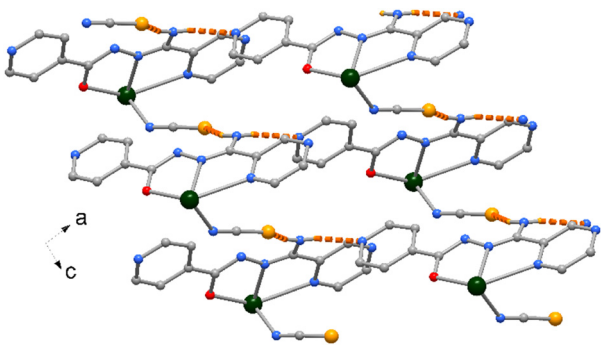

Fig. 4 2D polymeric layer formed by H-bond interactions in complex **2**.

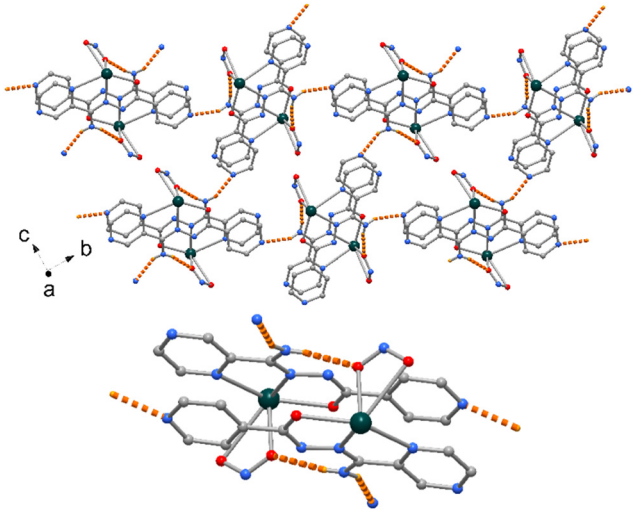

Fig. 5 Top: The double 2D polymeric layers built by H-bond interactions in complex **3**. Bottom: A detail of paired complexes unit.

complexes (*vide infra*). The MEP analysis shows a variety of electron-rich atoms apart from the pyridine N-atom and the pseudohalide ligands, which are the non-coordinated pyrimidine N-atom, the coordinated O-atom of the organic ligand (L) and the amidic N-atom, ranging from −15.7 to −22.6 kcal mol^{-1}. The MEP surfaces of compounds **3** and **4** are shown in Fig. 8, which are similar to those of compounds **1** and **2**. The main difference is in compound **4**, where the minimum is located at the nitrito ligand (−40.2 kcal mol^{-1}) instead of the pyridine N-atom (−38.3 kcal mol^{-1}) as observed in **1**–**3**.

Two tetrel bonding self-assembled dimers of compounds **1** and **2** have been studied using QTAIM analysis (see

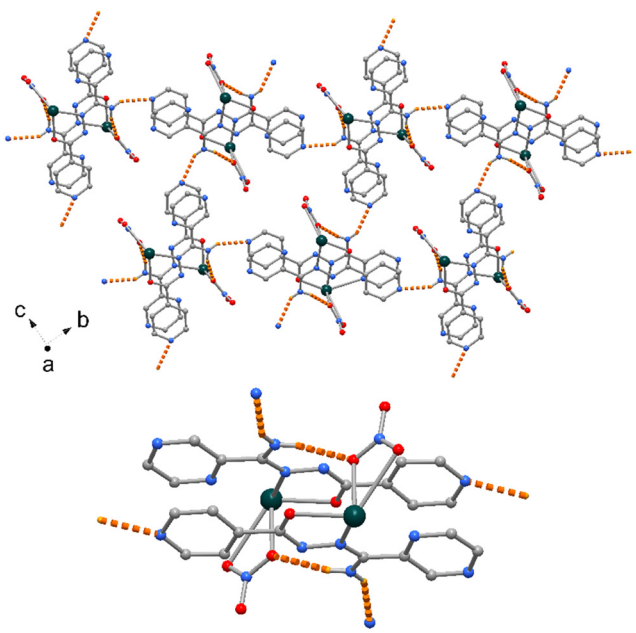

Fig. 6 Top: The double 2D polymeric layers built by H-bond interactions in complex **4**. Bottom: A detail of paired complexes unit.

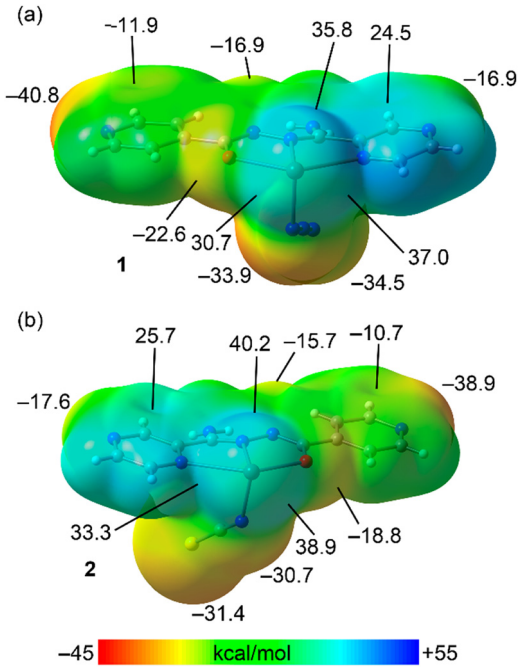

Fig. 7 MEP plotted onto the van der Waals surface of compounds **1** (a) and **2** (b) computed at the PBE0-D3/def2-TZP level of theory. The MEP values at selected points of the surfaces are indicated.

Fig. 9a, c, d and f). Moreover, two additional dimers extracted from 1D supramolecular chains of both compounds have been

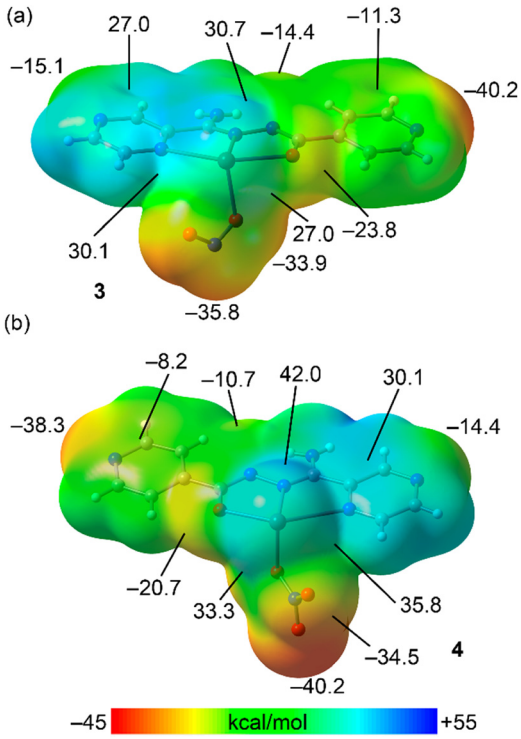

Fig. 8 MEP plotted onto the van der Waals surface of compounds **3** (a) and **4** (b) computed at the PBE0-D3/def2-TZP level of theory. The MEP values at selected points of the surfaces are indicated.

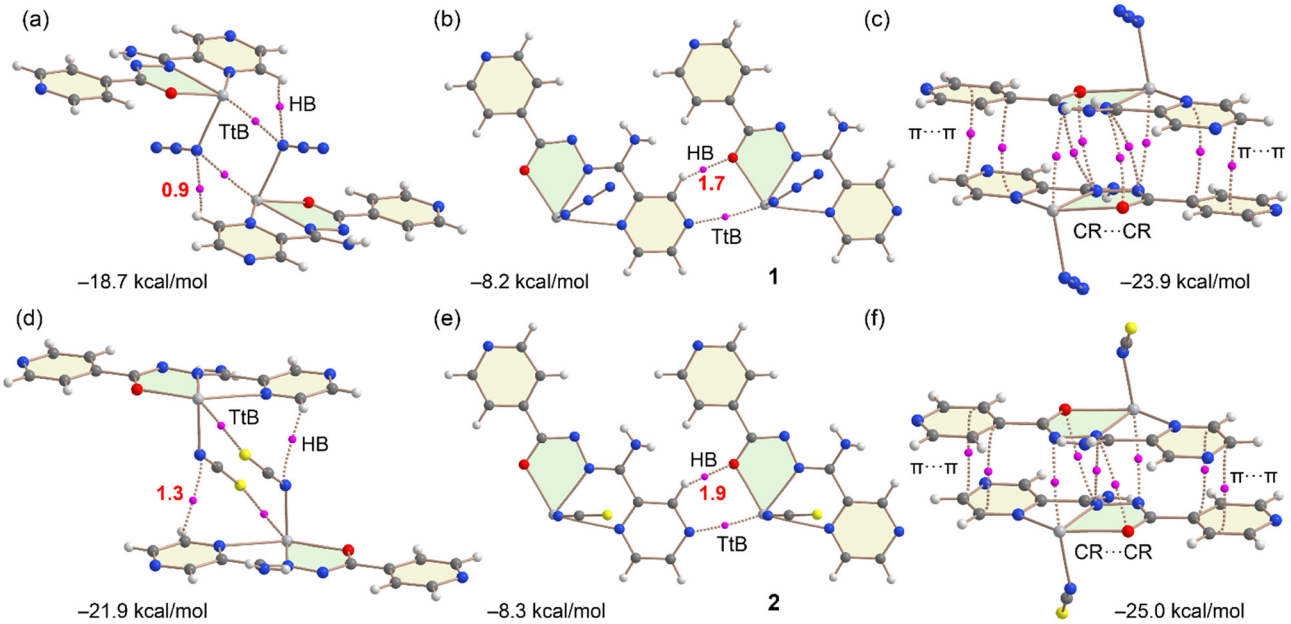

Fig. 9 AIM analyses of three dimers of complex **1** (a–c) and **2** (d–f). Bond critical points are represented by fuchsia spheres. The bond paths are represented by dashed lines. Only intermolecular interactions are represented. The dimerization energies are also indicated.

analyzed (see Fig. 9c and e). The energetic results and distribution of bond critical points (BCPs) and bond paths of all dimers are given in Fig. 9. The self-assembled dimers represented in Fig. 8a and d are formed by means of two symmetrically equivalent tetrel bonds (TtB) that are established between the lead atom and the N/S-atoms of the anionic co-ligands. Both exhibit considerable dimerization energies, −18.7 kcal mol^{-1} and −21.9 kcal mol^{-1} for **1** and **2**, respectively. The stronger binding energy observed for the dimer of **2** can be related to the more intense σ-hole (Fig. 7) and the larger contribution of the ancillary H-bonds. Than is, the QTAIM analysis not only shows the bond critical points (BCPs) and bond paths connecting the Pb and N,S-atoms but also reveals the existence of CH···N contacts involving aromatic CH bonds and the N-atoms of the pseudohalide coligands. In red font, the contribution of each H-bond is indicated, which was estimated using Espinosa's methodology.[54] It demonstrates that the HB is stronger in **2** (−1.3 kcal mol^{-1}) than in **1** (−0.9 kcal mol^{-1}), thus further contributing to the larger dimerization energy observed in **2**. The interaction energies of the antiparallel π-stacking dimers are considerable (−23.9 kcal mol^{-1} and −25.0 kcal mol^{-1}, respectively) in agreement with the MEP study that shows opposite signs for the MEP values over the coordinated pyridine and uncoordinated pyrazine rings. Consequently, these electrostatically enhanced π···π complexes are powerful binding motifs in the crystal structure. In fact, these motifs are common in all four structures (see Fig. 9 and 10). The QTAIM analysis (Fig. 9c and f) shows that the pyridine···pyrimidine stacking is characterized by two BCPs and bond paths interconnecting two atoms of the aromatic rings. The QTAIM analysis also shows BCPs and bond paths connecting the Pb-atoms to the N-atoms of the five-membered chelate rings (CRs). Additional BCPs and bond paths interconnect the chelate rings, thus disclosing that these rings are also active players in the π-binding mechanism and explain the large binding energies. Apart from the self-assembled dimers, both compounds form infinite 1D chains that propagate by means of N4···Pb TtBs (see Fig. 1 and Table 1).

Dimers extracted from the 1D supramolecular polymers are shown in Fig. 9b and e. The TtB is characterized by the corresponding BCP and bond path interconnecting the Pb and N-atoms. Moreover, the QTAIM analysis also reveals the presence of a concurrent CH···O interaction that contributes −1.7 kcal mol^{-1} in **1** and −1.8 kcal mol^{-1} to assembly. This energetic analysis evidences that the formation of these dimers (and consequently the 1D chains) is dominated by the tetrel bond, whose interaction energy is almost identical in both compounds (−6.5 and −6.4 kcal mol^{-1} in **1** and **2**, respectively). The studied tetrel bonded dimers of compounds **3** and **4** are given in Fig. 10. As commented above, both π-stacked self-assembled dimers are also observed in both compounds, evidencing that this is a concurrent and strong binding motif in all compounds. The interaction energies are similar to those computed for compounds **1** and **2**. Regarding the supramolecular 1D polymer propagated by tetrel bonds, it is only observed in compound **4**. That is, the N4···Pb distance is very long in compound **3**, 3.781 Å, see Table 1 (0.211 Å longer than the sum of van der Waals radii), and thus not considered in this study. In addition, the self-assembled TtB dimer involving the anionic coligand as the donor is only observed in compound **3**. It is worth mentioning that, in both compounds, the anionic coligand is bonded to the Pb-atom by a conventional coordination Pb–O bond and a noncovalent Pb···O tetrel bond, that is also represented in Fig. 10. This intramolecular contact diminishes the ability of Pb to establish intermolecular tetrel bonds, explaining the long N4···Pb

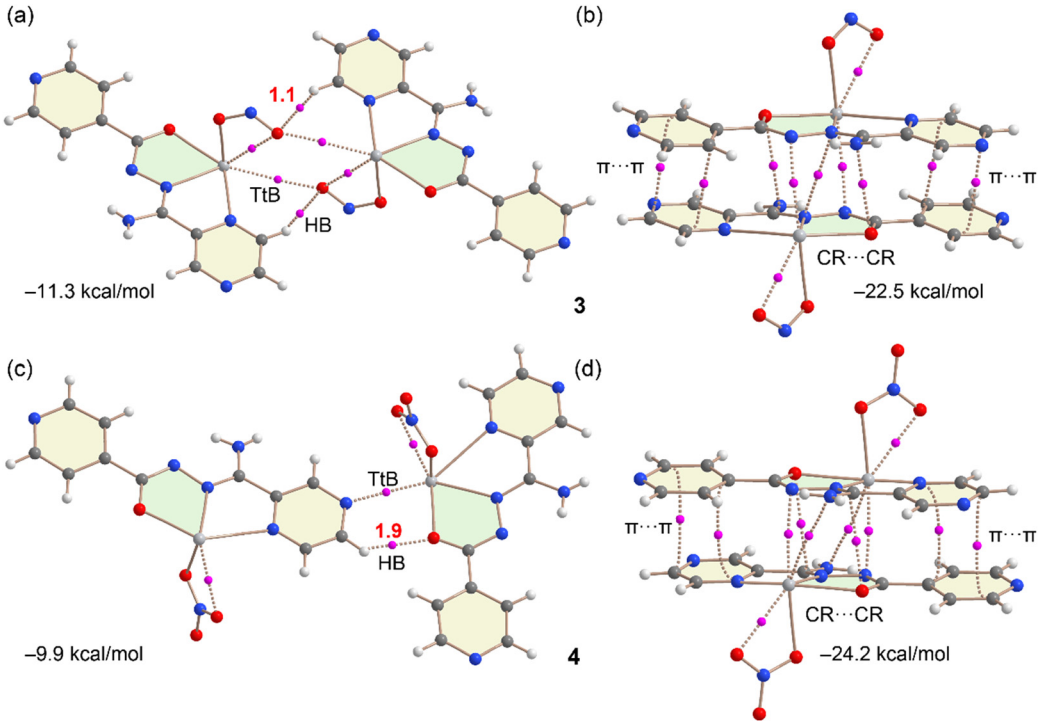

Fig. 10 AIM analyses of two dimers of complex **3** (a and b) and **4** (c and d). Bond critical points are represented by fuchsia spheres. The bond paths are represented by dashed lines. Only intermolecular interactions are represented apart from the intramolecular Pb···ON. The dimerization energies are also indicated.

distance in **3** and the absence of Pb···O(NO_3) contacts in **4**. It can be observed that in the TtB dimers of compounds **3** (Fig. 10a) and **4** (Fig. 10c), tetrel and hydrogen bonds are concurrently established. The contribution of the H-bond is −1.1 kcal mol^{-1} in **3** and −1.9 kcal mol^{-1} in **4**.

The binding energy of the self-assembled tetrel bonding dimer in **3** is −11.3 kcal mol^{-1} (Fig. 10a), which is significantly smaller than those of compounds **1** and **2** in line with the less intense σ-hole opposite to the Pb–O bond observed in **3** compared to **1** and **2**. This difference in the MEP value is most likely due to the influence of the intramolecular Pb···O(NO_2) interaction. The contour line diagrams of the Laplacian of electron density distribution $\nabla^2\rho(r)$, bond paths, visualization of reduced density gradient (RDG) and electron localization function (ELF) 2D maps for self-assembled TtB dimers of compounds **1–3** are shown in Fig. 11. These 2D maps along the QTAIM parameters at the BCPs evidence that the Pb···N,S,O contacts can be classified as noncovalent and similar to previously reported systems.[25–34] That is, the low magnitude of the electron density (0.0049–0.0156 a.u.), positive values of the Laplacian of electron density (0.0170–0.0380 a.u.), and positive values of total energy density ($G > |V|$) values are typical for weak noncovalent interactions. The Laplacian of electron density can be decomposed into the sum of contributions along the three principal axes of maximal variation, giving the three eigenvalues of the Hessian matrix (λ_1, λ_2, and λ_3). The sign of λ_2 can be utilized to distinguish bonding (attractive, $\lambda_2 < 0$) weak interactions from non-bonding ones (repulsive, $\lambda_2 > 0$).[47] Thus, all tetrel bonds are attractive in line with the binding energies.

The 2D ELF maps are also useful to confirm the σ-hole nature of the interaction. They clearly show that the bond paths characterizing the TtBs in **1–3** cross the LP at the electron donor atom (N, S, O) and the region around the Pb-atom where the ELF is significantly reduced (σ-hole), see Fig. 11.

Conclusions

In this study, we have successfully synthesized and characterized four novel lead(II) complexes with pyrazoylisonicotinoylhydrazone ligands, each paired with diverse anionic co-ligands. Through meticulous structural, analytical, and spectroscopic evaluations, we have revealed the unique ability of these complexes to form varied supramolecular structures significantly influenced by the nature of their anionic counterparts. The investigation into the hemidirectional coordination of lead within these complexes has shed light on the pivotal role of tetrel bonding in promoting the assembly of these molecular units into larger, complex architectures, ranging from self-assembled dimers to extensive one-dimensional polymers. Advanced computational analyses, including DFT calculations and a suite of computational tools like MEP, NCIPlot, QTAIM, and ELF methods, have further substantiated our understanding of the donor–acceptor dynamics and the critical interactions at play. This work not only contributes to the expanding knowledge of lead(II) coordination chemistry but also emphasizes the importance of tetrel bonding in the design and development of novel

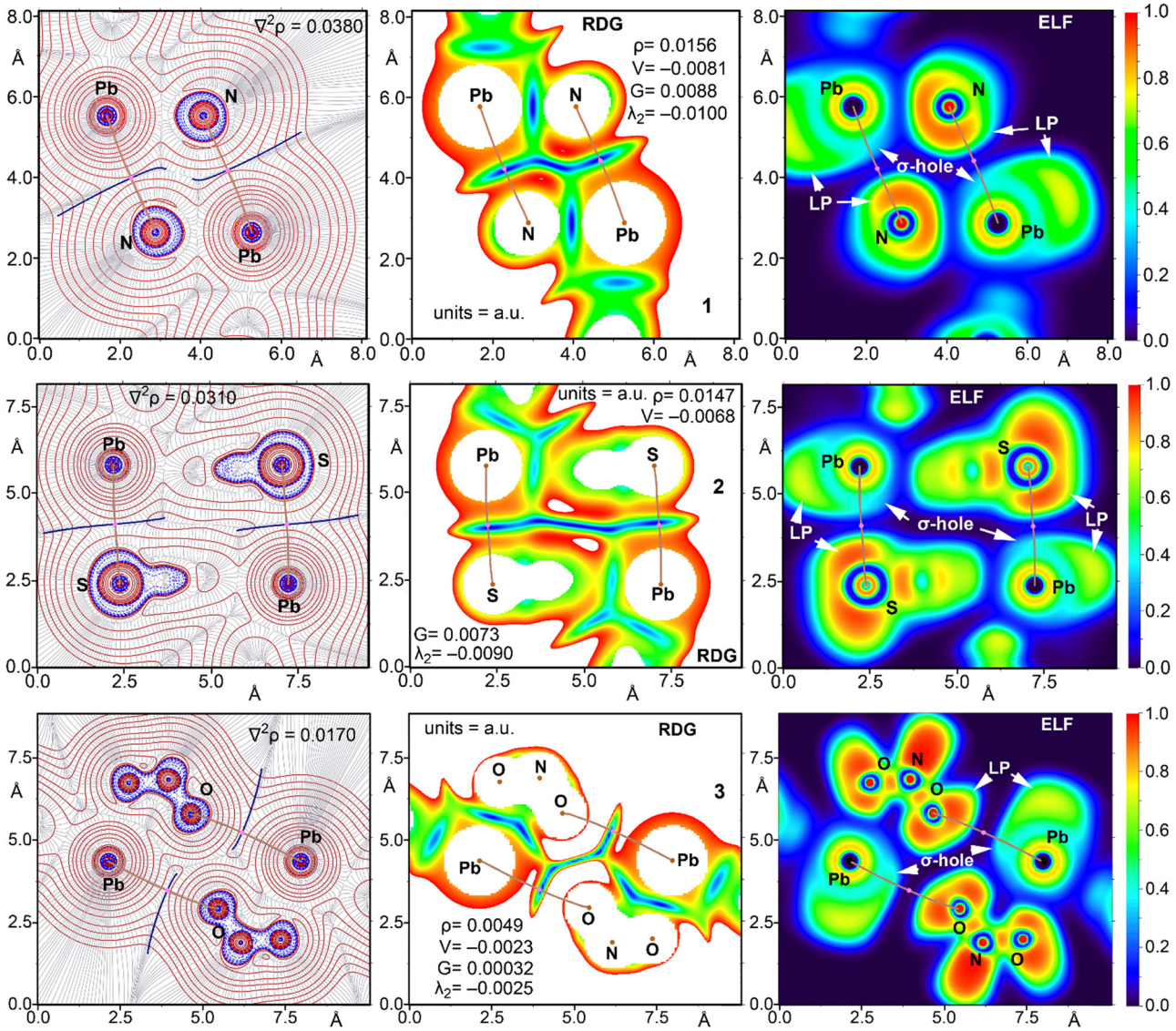

Fig. 11 Contour line diagram (positive values in red and negative in blue) of the Laplacian of electron density distribution $\nabla^2\rho(r)$, bond paths, (left panels), visualization of electron localization function (ELF, center panels), and reduced density gradient (RDG, right panels) analyses for tetrel bonding interactions in the X-ray structures **1** (top), **2** (middle) and **3** (bottom). Bond critical points (3, –1) are shown in pink and bond paths are shown as pale brown lines, and the colour scale for the ELF and RDG maps is presented in a.u.

supramolecular assemblies, opening avenues for future applications in materials science and catalysis.

Author contributions

The manuscript was collaboratively developed with contributions from all authors.

Conflicts of interest

There are no conflicts to declare.

Acknowledgements

We thank MICIU/AEI of Spain (PID2020-115637GB-I00, FEDER funds) for financial support, the CTI (UIB) for computational facilities. AF thanks the Alexander von Humboldt Foundation for the J. C. Mutis research award. I. G. S thanks to the financial support received from Consellería de Cultura, Educación, Formación Profesional e Universidades, Xunta de Galicia (Spain). GPC GI-2197 (ED481B-2022-068 2023/19).

Notes and references

1 J. Řezáč and P. Hobza, *Chem. Rev.*, 2016, **116**, 5038–5071.
2 F. Biedermann and H.-J. Schneider, *Chem. Rev.*, 2016, **116**, 5216–5300.
3 K. T. Mahmudov, M. N. Kopylovich, M. F. C. Guedes da Silva and A. J. L. Pombeiro, *Coord. Chem. Rev.*, 2017, **345**, 54–72.

4 P. Hobza and R. Zahradník, *Chem. Rev.*, 1988, **88**, 871–897.
5 K. Müller-Dethlefs and P. Hobza, *Chem. Rev.*, 2000, **100**, 143–168.
6 K. E. Riley, M. Pitoňak, P. Jurečka and P. Hobza, *Chem. Rev.*, 2010, **110**, 5023–5063.
7 K. E. Riley and P. Hobza, *Acc. Chem. Res.*, 2013, **46**, 927–936.
8 A. S. Mahadevi and G. N. Sastry, *Chem. Rev.*, 2016, **116**, 2775–2825.
9 *Halogen Bonding: Fundamentals and Applications*, ed. P. Metrangolo and G. Resnati, Springer, Berlin, 2008.
10 *Halogen Bonding I: Impact on Materials Chemistry and Life Sciences*, ed. P. Metrangolo and G. Resnati, Springer International Publishing, Cham, 2015.
11 G. R. Desiraju, P. S. Ho, L. Kloo, A. C. Legon, R. Marquardt, P. Metrangolo, P. Politzer, G. Resnati and K. Rissanen, *Pure Appl. Chem.*, 2013, **85**, 1711.
12 G. Cavallo, P. Metrangolo, T. Pilati, G. Resnati and G. Terraneo, *Cryst. Growth Des.*, 2014, **14**, 2697.
13 A. Bauzá, T. J. Mooibroek and A. Frontera, *ChemPhysChem*, 2015, **16**, 2496.
14 C. B. Aakeroy, D. L. Bryce, G. R. Desiraju, A. Frontera, A. Legon, F. Nicotra, K. Rissanen, S. Scheiner, G. Terraneo, P. Metrangolo and G. Resnati, *Pure Appl. Chem.*, 2019, **91**, 1889–1892.
15 G. Resnati, D. L. Bryce, G. R. Desiraju, A. Frontera, I. Krossing, A. C. Legon, P. Metrangolo, F. Nicotra, K. Rissanen, S. Scheiner and G. Terraneo, *Pure Appl. Chem.*, 2024, **96**, 135–145.
16 (*a*) P. R. Varadwaj, A. Varadwaj, H. M. Marques and K. Yamashita, *CrystEngComm*, 2023, **25**, 1411, and references cited therein; (*b*) A. Bauzá, T. J. Mooibroek and A. Frontera, *Angew. Chem., Int. Ed.*, 2013, **52**, 12317.
17 A. Bauzá and A. Frontera, *Angew. Chem., Int. Ed.*, 2015, **54**, 7340.
18 IUPAC Project 2016-001-2-300: Categorizing Chalcogen, Pnictogen, And Tetrel Bonds, And Other Interactions Involving Groups 14–16 Elements, **https://iupac.org/projects/project-details/?project_nr=2016-001-2-300**.
19 P. Politzer, J. S. Murray and T. Clark, *Phys. Chem. Chem. Phys.*, 2013, **15**, 11178.
20 J. S. Murray, P. Lane and P. Politzer, *J. Mol. Model.*, 2009, **15**, 723–729.
21 J. S. Murray, K. E. Riley, P. Politzer and T. Clark, *Aust. J. Chem.*, 2010, **63**, 1598–1607.
22 P. Politzer and J. S. Murray, *ChemPhysChem*, 2013, **14**, 278.
23 A. Bauzá, T. J. Mooibroek and A. Frontera, *Chem. Rec.*, 2016, **16**, 473.
24 A. Bauzá, S. K. Seth and A. Frontera, *Coord. Chem. Rev.*, 2019, **384**, 107–125.
25 M. S. Gargari, V. Stilinović, A. Bauzá, A. Frontera, P. McArdle, D. Van Derveer, S. W. Ng and G. Mahmoudi, *Chem. – Eur. J.*, 2015, **21**, 17951.
26 G. Mahmoudi, A. Bauzá, A. Frontera, P. Garczarek, V. Stilinović, A. M. Kirillov, A. Kennedy and C. Ruiz-Pérez, *CrystEngComm*, 2016, **18**, 5375.
27 G. Mahmoudi, A. Bauzá, M. Amini, E. Molins, J. T. Mague and A. Frontera, *Dalton Trans.*, 2016, **45**, 10708.
28 G. Mahmoudi, D. A. Safin, M. P. Mitoraj, M. Amini, M. Kubicki, T. Doert, F. Locherer and M. Fleck, *Inorg. Chem. Front.*, 2017, **4**, 171.
29 G. Mahmoudi, A. Bauzá and A. Frontera, *Dalton Trans.*, 2016, **45**, 4965.
30 S. Mirdya, A. Frontera and S. Chattopadhyay, *CrystEngComm*, 2019, **21**, 6859.
31 F. A. Afkhami, G. Mahmoudi, F. Qu, A. Gupta, M. Köse, E. Zangrando, F. I. Zubkov, I. Alkorta and D. A. Safin, *CrystEngComm*, 2020, **22**, 2389.
32 G. Mahmoudi, F. A. Afkhami, A. R. Kennedy, F. I. Zubkov, E. Zangrando, A. M. Kirillov, E. Molins, M. P. Mitoraj and D. A. Safin, *Dalton Trans.*, 2020, **49**, 11238.
33 I. Garcia-Santos, T. Iglesias-Pereiro, E. Labisbal, A. Castiñeiras, B. Eftekhari-Sis, G. Mahmoudi, F. Sagan, M. P. Mitoraj and D. A. Safin, *CrystEngComm*, 2024, **26**, 1252.
34 S. A. Southern, D. Errulat, J. M. Frost, B. Gabidullin and D. L. Bryce, *Faraday Discuss.*, 2017, **203**, 165.
35 Bruker, *APEX3 Software, v2019.11-0*, Bruker AXS Inc., Madison, Wisconsin, USA, 2019.
36 G. M. Sheldrick, *SADABS. Program for Empirical Absorption Correction of Area Detector Data*, University of Goettingen, Germany, 1997.
37 G. M. Sheldrick, *Acta Crystallogr., Sect. A: Found. Crystallogr.*, 2008, **64**, 112–122.
38 K. Brandenburg and H. Putz, *DIAMOND*, Crystal Impact GbR, Bonn, Germany, 1999.
39 L. J. Farrugia, *J. Appl. Crystallogr.*, 2012, **45**, 849–854.
40 C. Adamo and V. Barone, *J. Chem. Phys.*, 1999, **110**, 6158–6170.
41 E. Caldeweyher, C. Bannwarth and S. Grimme, *J. Chem. Phys.*, 2017, **147**, 034112.
42 F. Weigend, *Phys. Chem. Chem. Phys.*, 2006, **8**, 1057–1065.
43 M. J. Frisch, G. W. Trucks, H. B. Schlegel, G. E. Scuseria, M. A. Robb, J. R. Cheeseman, G. Scalmani, V. Barone, G. A. Petersson, H. Nakatsuji, X. Li, M. Caricato, A. V. Marenich, J. Bloino, B. G. Janesko, R. Gomperts, B. Mennucci, H. P. Hratchian, J. V. Ortiz, A. F. Izmaylov, J. L. Sonnenberg, D. Williams-Young, F. Ding, F. Lipparini, F. Egidi, J. Goings, B. Peng, A. Petrone, T. Henderson, D. Ranasinghe, V. G. Zakrzewski, J. Gao, N. Rega, G. Zheng, W. Liang, M. Hada, M. Ehara, K. Toyota, R. Fukuda, J. Hasegawa, M. Ishida, T. Nakajima, Y. Honda, O. Kitao, H. Nakai, T. Vreven, K. Throssell, J. A. Montgomery, Jr., J. E. Peralta, F. Ogliaro, M. J. Bearpark, J. J. Heyd, E. N. Brothers, K. N. Kudin, V. N. Staroverov, T. A. Keith, R. Kobayashi, J. Normand, K. Raghavachari, A. P. Rendell, J. C. Burant, S. S. Iyengar, J. Tomasi, M. Cossi, J. M. Millam, M. Klene, C. Adamo, R. Cammi, J. W. Ochterski, R. L. Martin, K. Morokuma, O. Farkas, J. B. Foresman and D. J. Fox, *Gaussian 16, Revision C.01*, Gaussian, Inc., Wallingford CT, 2016.
44 S. F. Boys and F. Bernardi, *Mol. Phys.*, 1970, **19**, 553–566.
45 R. F. W. Bader, *Chem. Rev.*, 1991, **91**, 893–928.

46 T. A. Keith, *AIMAll (Version 13.05.06)*, TK Gristmill Software, Overland Park KS, USA, 2013.
47 J. Contreras-Garcia, E. R. Johnson, S. Keinan, R. Chaudret, J.-P. Piquemal, D. N. Beratan and W. Yang, *J. Chem. Theory Comput.*, 2011, **7**, 625–632.
48 A. D. Becke and K. E. Edgecombe, *J. Chem. Phys.*, 1990, **92**, 5397–5403.
49 T. Lu and F. Chen, *J. Comput. Chem.*, 2012, **33**, 580–592.
50 G. Mahmoudi, M. Abedi, S. E. Lawrence, E. Zangrando, M. G. Babashkina, A. Klein, A. Frontera and D. A. Safin, *Molecules*, 2020, **25**, 4056.
51 G. Mahmoudi, D. A. Safin, M. P. Mitoraj, M. Amini, M. Kubicki, T. Doert, F. Locherere and M. Fleck, *Inorg. Chem. Front.*, 2017, **4**, 171–182.
52 G. Mahmoudi, A. Masoudiasl, F. A. Afkhami, J. M. White, E. Zangrando, A. V. Gurbanov, A. Frontera and D. A. Safin, *J. Mol. Struct.*, 2021, **1234**, 130139.
53 G. Mahmoudi, E. Zangrando, M. P. Mitoraj, A. V. Gurbanov, F. I. Zubkov, M. Moosavifar, I. A. Konyaeva, A. M. Kirillov and D. A. Safin, *New J. Chem.*, 2018, **42**, 4959–4971.
54 E. Espinosa, E. Molins and C. Lecomte, *Chem. Phys. Lett.*, 1998, **285**, 170–173.